Conditions for convective deep inflow

Yi-Hung Kuo & J. David Neelin

Department of Atmospheric and Oceanic Sciences, University of California, Los Angeles, CA 90095

Key Points:

- Observations and simulations point to a common structure of convective mass flux drawing air from a deep layer in the lower troposphere
- Most deep-convective precipitation comes from features with horizontal size comparable to or exceeding the lower tropospheric depth
- For these, the nonlocal response of convective updrafts to buoyancy provides a simple explanation for the observed deep-inflow structure

Corresponding author: Yi-Hung Kuo, yhkuo@atmos.ucla.edu

Abstract

Observations and cloud-resolving simulations suggest that a convective updraft structure drawing mass from a deep lower-tropospheric layer occurs over a wide range of conditions. This occurs for both mesoscale convective systems (MCSs) and less-organized convection, raising the question: Is there a simple, universal characteristic governing the deep inflow? Here we argue that nonlocal dynamics of the response to buoyancy are key. For precipitating deep-convective features including horizontal scales comparable to a substantial fraction of the troposphere depth, the response to buoyancy tends to yield deep inflow into the updraft mass flux. Precipitation features in this range of scales are found to dominate contributions to observed convective precipitation for both MCS and less-organized convection. The importance of such nonlocal dynamics implies thinking beyond parcel models with small-scale turbulence for representation of convection in climate models. Solutions here lend support to investment in parameterizations at a complexity between conventional and superparameterization.

Plain Language Summary

Deep convection, whether in isolated thunderstorms or organized mesoscale convective systems, is a leading effect in climate dynamics and climate change, yet it remains subject to large uncertainties in climate models. The way that air enters convective clouds plays a substantial role in this uncertainty, and recently the importance of inflow through a deep layer in the lower troposphere has been noted, although why this should apply for both isolated and organized convection has been unclear. Here we show that an aspect of dynamics omitted from conventional climate model representations provides a simple explanation for this for large clouds that account for most convective precipitation. This suggests physical effects requiring substantial revisions in climate models.

1 Introduction

Accurate simulation and forecasting of weather and climate depends on adequate representations of deep convection in general circulation models (GCMs). This remains a challenging subject (Randall et al., 2003; Kuo et al., 2020; Leung et al., 2022) even with the advances in cloud-resolving models (CRMs) and machine learning (Wing et al., 2020; Bretherton et al., 2021). Challenges arise especially in regards to (i) organized convection, such as mesoscale convective systems (MCSs) (Moncrieff et al., 2012; Yano & Moncrieff, 2016) that account for a significant fraction of precipitation (Nesbitt et al., 2006); and (ii) the entrainment process of environmental air entering in-cloud updrafts (Plant, 2010; Sherwood et al., 2014). The traditional view of entrainment assumes a plume/parcel rising from near the surface that is modified by its immediate surroundings via localized, small-scale turbulent mixing (Arakawa & Schubert, 1974). This motivated efforts to quantify a postulated local entrainment rate (Siebesma et al., 2003; Del Genio & Wu, 2010; Masunaga & Luo, 2016)—primarily by indirect means—from which mass flux can be derived for plume models in parameterization schemes (de Rooy & Siebesma, 2010; Morrison, 2017). At odds with the above conceptual model, a range of turbulent scales contributes to the mixing within actual convective entities, and features of larger scales are instrumental for nonlocal transport by convection (Siebesma et al., 2007).

Field measurements of convective updrafts during aircraft campaigns (LeMone & Zipser, 1980; Lucas et al., 1994) and by radar wind profilers (Schiro et al., 2018; Savazzi et al., 2021), in accordance with CRM simulations (Robe & Emanuel, 1996; Li et al., 2008), identify a common mass flux structure that gradually increases throughout the lower troposphere. Contributions to this can occur through coherent inflow (Moncrieff, 1992)—termed dynamic entrainment (Houghton & Cramer, 1951; Ferrier & Houze, 1989)—in contrast with the conventional paradigm of small-scale mixing. Deep-inflow profiles, with environmental air entering the updraft through a deep lower-tropospheric layer, can also

be inferred from the dependence of precipitation on the temperature-moisture environment as a function of lower-tropospheric layer (Ahmed & Neelin, 2018). The deep-inflow profile is in general agnostic as to whether inflow occurs by spatially coherent flow, small-scale turbulence, or both.

Given the importance of mass flux in convective parameterizations, the occurrence of simple vertical structures demands explanation, particularly since any potential for directly constraining such structures could aid in bypassing the elusive task of determining vertical dependence of entrainment rate (Kuang & Bretherton, 2006; Romps, 2010). The apparent widespread occurrence of deep-inflow structures, together with the surprising observation that such structures occur similarly for both MCS and less-organized deep convection (Schiro et al., 2018), raises the question of whether there is some universal characteristic governing the dynamics of deep inflow.

Here we adapt elements from the anelastic modeling literature to show how they may provide an explanation for this specific physical phenomenon. As prelude, section 2 reviews evidence for deep inflow, previews the potential role of nonlocal solutions, and provides an observational analysis that indicates the range of horizontal scales in convective precipitation features. We then recap anelastic equations for the response to buoyancy, cast in a form suitable for vertical acceleration (section 3), and show the implications for vertically nonlocal response for a given wavelength. In section 4, we examine response to horizontally localized buoyancy features while demonstrating robustness to smaller scale variations. Finally we discuss the conditions under which the nonlocal solution provides a simple explanation for deep inflow and implications for convective parameterizations based on parcel models that neglect these effects.

2 Convective precipitation feature scales and inflow

Fig. 1 provides an overview of key ingredients of the deep-inflow problem and of the proposed solution. First, Fig. 1a summarizes the observed deep-convective updrafts in the lower troposphere. The gradual increase of mass flux with height implies horizontal convergence of environmental air into the updraft through much of the lower troposphere. Such mass flux profiles are characteristic of both MCS and less-organized convection.

Second, Fig. 1b provides a thumbnail of key results from the nonlocal response to buoyancy elaborated in subsequent sections. For localized net-positive buoyancy structures of horizontal diameter D and vertical extent $4 \leq z \leq 8$ km, the nonlocal response of mass flux $\partial_t(\rho_0 \bar{w})$ averaged within the diameter yields a deep-inflow profile through the lower troposphere. This tends to converge to a roughly linear increase for a broad range of reasonable conditions when D is comparable to the depth of the tropospheric layer under consideration.

Third, in Fig. 1c we quantify the claim that much of the deep-convective precipitation comes from features that include such horizontal scales (Appendix A). Contiguous features of convective precipitation are identified from satellite precipitation radar (PR) retrievals. The contribution to total convective precipitation is shown as a function of feature size estimated two different ways: by cord length of the feature and by square root of the area of the feature. The contribution to convective precipitation is further separated by features that meet common criteria for MCS, and less-organized features that do not. Note that stratiform precipitation is *not* included, since we wish to focus on the scales of features of the deep-convective precipitation. For both MCS and less-organized convection, the precipitation contribution peaks around 15 km, and $> 70\%$ of the total convective rain is from events of this scale or greater for both feature size measures. That is, convective rain is mostly from deep-convective features whose horizontal extent is comparable to the depth of the troposphere. MCS features tend to have

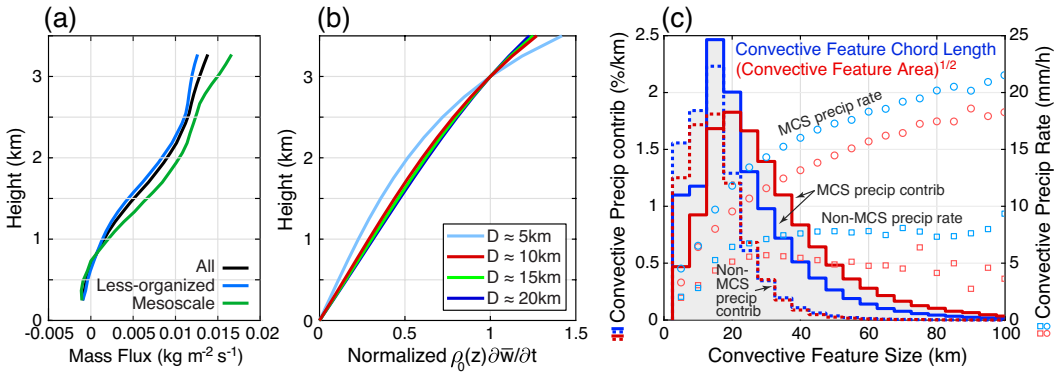

Figure 1. (a) Mean deep-convective updraft mass flux profiles in the lower troposphere for mesoscale, less-organized, and all precipitating convective events estimated from radar wind profiler during the GOAmazon campaign adapted from Schiro et al. (2018). (b) Theoretical response of convective mass flux to buoyancy tartares of vertical extent $4 \leq z \leq 8$ km and varying horizontal diameter D. The tartares consist of randomly-generated small cylindrical bubbles with a 7:3 warm-to-cold bubble ratio (see Fig. 4a). The response profiles are the mean within the diameter D and averaged over an ensemble of 10 tartare realizations, then normalized using values at $z = 3$ km. (c) Convective precipitation contribution (curves) and precipitation rate (markers), for MCS and non-MCS features, conditioned on convective feature size measured by chord length (blue) and square root of area (red). The areas under the MCS and non-MCS precipitation contribution curves sum to unity. Feature size is solely based on contiguous *convective* precipitation pixels.

greater contribution to convective rain at large sizes than do less-organized features. While the conditionally averaged convective precipitation rate for less-organized features (squares) levels off as size exceeds ∼25 km, the MCS precipitation rate (circles) continues to increase asymptotically as roughly the 1/4-th power of size.

The convective precipitation region is not necessarily identical to that of the buoyancy, but provides a rough measure of the existence of strong updrafts and downdrafts indicative of buoyancy anomalies. The spatiotemporal coverage of the satellite PR provides regions and periods extensive enough to identify typical characteristics of convection. We also note that the PR resolution ∼5 km coarse-grains smaller scale variations, but suffices to support that localized features containing substantial convective rain occur over a broad range of scales. The nonlocal effects discussed below also help justify such coarse-graining.

We thus have 1) observational evidence that much of the convective rain in both MCS and less-organized systems comes from features with characteristic sizes of the convection exceeding ∼10 km; and 2) a theoretical basis for how the nonlocal nature of the response to buoyancy tends to yield deep inflow on such scales.

3 Nonlocal response to buoyancy

We follow the anelastic framework (Ogura & Phillips, 1962) to derive the diagnostic equation for the response to buoyancy. The anelastic approximation assumes a horizontally homogeneous, time-invariant atmospheric density $\rho_0(z)$, allowing the governing system to filter acoustic waves and retain nonhydrostatic solutions relevant for deep convection with $O(1)$ aspect ratio (Markowski & Richardson, 2011). Thus the anelas-

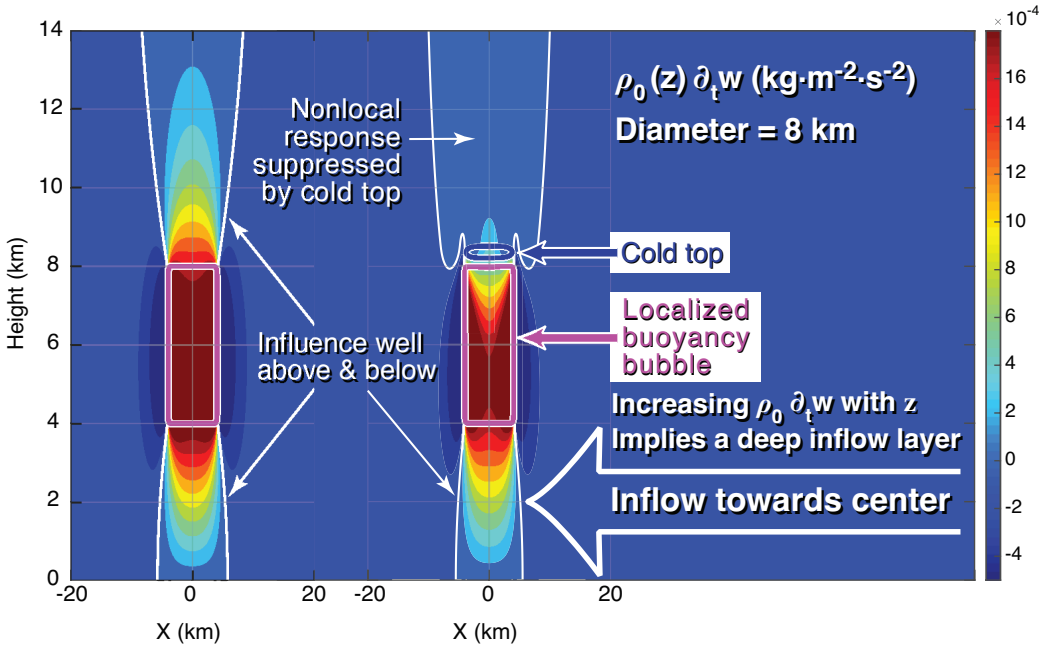

Figure 2. Cross section of vertical mass flux response (color shading; kg/m^{2}s^2) to idealized buoyancy forcing with constant $B = 0.01$ m/s^2 in cylindrical bubbles of 8-km diameter (magenta contours). The case on the right also includes a negatively buoyant region immediately above ($B = -0.06$ m/s^2) to illustrate the tendency of the "convective cold top" to cancel vertical motion above the main updraft. The white contours indicate zero response. The colorbar range is chosen to highlight details below and above the bubbles. See *section S3* for numerical details.

tic approximation has been widely adopted by CRMs (Bryan & Fritsch, 2002; Khairoutdinov & Randall, 2003; Jung & Arakawa, 2008).

3.1 Anelastic response to buoyancy field

With vorticity and anelastic continuity equations, one can derive (see *SI section S1*)

$$\nabla_h^2 a + \frac{\partial}{\partial z}\left[\frac{1}{\rho_0}\frac{\partial}{\partial z}(\rho_0 a)\right] = \nabla_h^2 B + \mathcal{D}, \tag{1}$$

where $a \equiv \partial_t w$ is the vertical acceleration, B the buoyancy, and $\mathcal{D}$ a quadratic function of spatial derivatives of velocity $\mathbf{u}$ (i.e., associated with flow kinematics) that vanishes when $\mathbf{u} \equiv 0$. The influences of buoyancy and kinematics on a can thus be separately diagnosed. Here we focus on the response to buoyancy, which allows a direct contrast to conventional parameterizations.

In Eq. (1), the operator acting on a is elliptic, one thus expects a global response even for localized forcing (Houze, 1993). The response is accompanied by adjustment to horizontal convergence driven by locally hydrostatic pressure gradients (Jeevanjee & Romps, 2016) to ensure mass conservation. Note that buoyancy drives acceleration via $\nabla_h^2 B$—flow evolves following horizontal variation of buoyancy.

To give a concrete sense of the nonlocal dynamics, Fig. 2 demonstrates two examples of the mass flux response $\rho_0 a$ (color shading) to idealized cylindrical buoyancy bubbles of 8-km diameter (magenta contours). Here a is from solving Eq. (1) (with $\mathcal{D} \equiv 0$)

for the two cases separately. The localized buoyancy generates strong upward acceleration within its diameter, accompanied by weak, broad downward acceleration in the surroundings. The extensive response reaches well below and above the bubble, driving a layer of flow into the convective region in the lower troposphere, as a consequence of gradually increasing $\rho_0 a$ with height, and outflow aloft from decreasing $\rho_0 a$. Other things equal, deeper bubbles generally result in greater response.

The nonlocal responses in Fig. 2 result from the elliptic operator in Eq. (1), and are well-known in principle (Cotton et al., 2010; Trapp, 2013). If the vertical velocity extends above the region where condensational heating can balance work against stratification (roughly the parcel-theory level of neutral buoyancy), a negative buoyancy tendency will occur. This results in the convective cold-top phenomenon (Holloway & Neelin, 2007), with a region of negative buoyancy tending to cancel the response above, as illustrated on the right in Fig. 2. Here we focus on the properties of the nonlocal solution within and below the positively buoyant region. If this part of the updraft is saturated (above an unstratified boundary layer), latent heating tends to cancel negative buoyancy tendencies. Building on previous work, we can then ask under what conditions the nonlocal solutions might provide an explanation for the deep inflow, and what physics this suggests might be missing from parcel models.

3.2 Analytic vertical structures

For a more detailed characterization of the nonlocal dynamics, we apply a Fourier transform to Eq. (1)

$$-\frac{4\pi^2}{L^2}\widehat{a} + \frac{\partial}{\partial z}\left[\frac{1}{\rho_0}\frac{\partial}{\partial z}(\rho_0 \widehat{a})\right] = -\frac{4\pi^2}{L^2}\widehat{B}, \tag{2}$$

where $a \sim \widehat{a}(z;k,\ell)e^{2\pi i(kx+\ell y)}$, $B \sim \widehat{B}(z;k,\ell)e^{2\pi i(kx+\ell y)}$, and $L \equiv (k^2+\ell^2)^{-1/2}$ is the horizontal wavelength.

Consider a simple buoyancy structure with $\widehat{B}(z) \equiv$ *constant* within a layer and vanishing elsewhere—general profiles can be approximated by superposition. We can analytically solve Eq. (2) (*section S2*) for the homogeneous solutions

$$\widehat{a}^{\pm}(z;k,\ell) \sim e^{\pm 2\pi z/L}, \tag{3}$$

and for the particular solution within the buoyant layer

$$\widehat{a}^{p}(z;k,\ell) \approx \widehat{B}(z;k,\ell). \tag{4}$$

The monochromatic (single-wavelength) solutions can then be constructed as a piecewise linear combination of $\widehat{a}^{\pm}$ and $\widehat{a}^{p}$ by matching across layer boundaries, yielding solutions similar to Jeevanjee (2017). Each horizontal wavelength gives rise to a vertical e-folding scale $H_s \equiv L/2\pi$—longer wavelength results in a greater range of nonlocal influence.

Fig. 3a shows examples of $\widehat{a}$ (lines) given a buoyant layer of depth $H_B = 1$ km and $\widehat{B} = 0.01$ m/s^2 (shadings) at various heights with $L = 5$ km. Above the buoyancy, the vanishing condition requires that $\widehat{a} \sim e^{-2\pi z/L}$. Below the buoyancy for layers away from the surface (compared with H_s), $\widehat{a} \sim e^{+2\pi z/L}$, and the overall profiles appear to be symmetric in z with maximum occurring in the middle of the layers. But for a layer at low altitude, the surface boundary condition results in $\widehat{a} \approx c_1 e^{+2\pi z/L} - c_2 e^{-2\pi z/L}$—adding $\widehat{a}^{p}$ if the layer reaches the surface—causing an approximately linear dependence on height below the maximum as well as an overall weaker response magnitude. This surface control is generally important for sufficiently long wavelength (see also Fig. 3b, blue line).

To further illustrate how the layer depth and horizontal wavelength affect the solutions, Fig. 3b includes additional examples for a deeper layer of buoyancy ($H_B = 6$

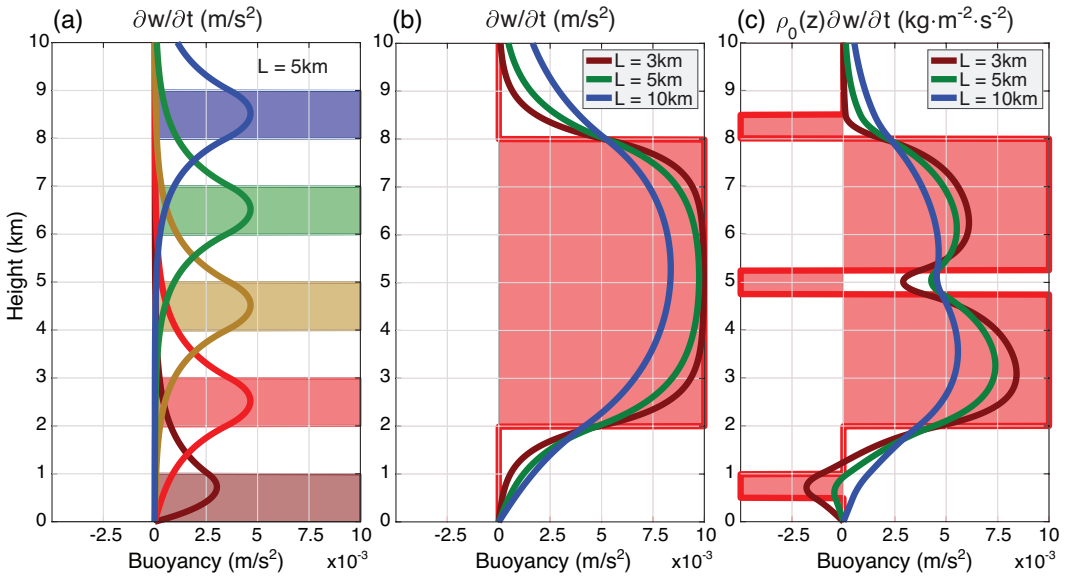

Figure 3. (a) Monochromatic solutions of vertical velocity response (lines) to individual buoyant layers located at different heights (shadings) with horizontal wavelength $L = 5$ km. (b) As in (a), for a deeper layer (red) and varying L. (c) As in (b), with additional thin layers of negative buoyancy, for vertical mass flux response. See *section S2* for numerical details.

km; red) and varying L. Short wavelength ($L/H_B \ll 1$) leads to limited nonlocal influence, mostly confined in the vicinity of the layer boundaries (brown line). Conversely, long wavelength and/or relatively shallow layer ($L/H_B \gg 1$) would yield solutions extending well outside the buoyant layer with reduced magnitude (blue line; also contrast with Fig. 3a). The aspect-ratio dependence is consistent with prior studies (Jeevanjee & Romps, 2016; Morrison, 2016), but for deep-inflow applications, L relative to a typical distance from the surface is important. Note also that the inflow can also continue for a characteristic vertical scale $\sim H_s$ within the buoyant layer. The mass flux responses corresponding to the accelerations in Figs. 3a,b are similar but bottom-heavier since ρ_0 decreases with height.

For a more sophisticated case, Fig. 3c shows the mass flux responses $\rho_0\widehat{a}$ (lines) to an idealized deep-convective structure with the addition of (i) a near-surface convective inhibition (CIN) layer; (ii) a thin negatively-buoyant layer representing, e.g., effects of melting near freezing level; and (iii) a layer resembling the convective cold-top. For short wavelength, the response tracks the variation of buoyancy. But for sufficient horizontal scales, the solution due to net-positive buoyancy has no difficulty tunneling through vertically restricted layers of negative buoyancy or near-surface CIN layer. The cold-top used here is sufficient to limit the vertical extent of the updraft for the shortest wavelength, but would need to be more intense for the longer wavelengths.

This last observation—based on a monochromatic argument but also supported by the solutions in section 4—has practical implications. First, this helps understand why a nighttime CIN layer may not prevent pre-existing storms from moving into a region, e.g., over the Mississippi basin or the Amazon (Burleyson et al., 2016): the layer depth plus surface interactions limit the effect of CIN. This may also be relevant to elevated MCSs (Marsham et al., 2011). Second, it addresses a common issue in parcel computations of convective available potential energy (CAPE) that have to contend with small layers in which parcel buoyancy goes negative (e.g., similar to the buoyancy in Fig. 3c)—

this can give rise to an underestimate of the energy actually available to convective storms; the results here indicate why updrafts in large storms easily penetrate such layers.

To briefly summarize the monochromatic dependence on scales: 1) the dependence is non-monotonic; the horizontal wavelength L determines the range of nonlocal vertical influence; small L yields the familiar limit of vertically localized response, while buoyancy layers that are thin compared to $L/2\pi$ yield response of limited magnitude. 2) L comparable to or exceeding a substantial fraction of the troposphere depth or of the height of the buoyant layer above the surface yields deep-inflow structure in the lower troposphere.

4 Buoyancy Tartare—robustness to fine structures

Two important modifications occur as one moves from considering a single wavelength to more realistic cases. First, the buoyancy associated with convective updrafts tends to be localized. Features of a finite horizontal size D and net-positive buoyancy consist of Fourier component contributions from a broad range of wavelength, primarily $L \gtrsim D$ (*section S4*). This includes nonlocal effects beyond what one would anticipate from the monochromatic considerations above, and is in contrast with prior studies that emphasized the contribution from $L \approx D$ (Jeevanjee, 2017). Second, robustness to complex buoyancy structures associated with imperfectly mixed turbulent flow must be assessed.

To address this, we build net-positive buoyancy patches from an ensemble of smaller elements, using the shorthand "tartare" to describe these constructions of larger scale D from "minced" ingredients of size $d \ll D$. Figs. 4a,c display two such tartares of diameter $D \approx 10$ km consisting of warm (red) and cold (blue) bubbles of $d = 1$ km and depth 0.5 km. In the first set of examples (as in Fig. 4a) the tartares are constructed to illustrate the nonlocal influence below the buoyancy by placing them at a distance from the surface. The mean mass flux responses to 10 randomly generated tartares for each D are demonstrated in Fig. 4b (depth indicated by gray shading). Through interference, the integral of individual d-bubbles leads to primary Fourier contributions from $L \gtrsim D$ for each D-tartare (*Fig. S1*). Thus for larger D or further below the buoyancy forcing, the responses converge towards linear dependence on height; see also Fig. 1b. For smaller D (e.g., $D \approx 5$ km) and closer to the forcing, the vertically localized behaviors—more rapid increase with height near the tartare base—from the smaller-scale $1 \lesssim L \lesssim 5$ km Fourier components can be distinguished from the nonlocal, roughly-linear solutions at lower height ($z < 2.5$ km) that are dominated by contributions from $L \gtrsim 5$ km.

Figs. 4c,d offer additional examples for tilted tartares—to mimic storms under windshear—with a greater depth and lower base. The tilt does not greatly alter the nonlocal behavior for D exceeding a substantial fraction of the tropospheric depth. Since the tartare base is at $z = 2$ km, the responses appear roughly linear even for $D \approx 5$ km. In a more comprehensive setup where the evolution of buoyancy is included, the tilt impacts the location of rain, hence cooling by evaporation of raindrops relative to latent heating. Here, the point is simply that tilted convective systems are subject to the same nonlocal dynamics.

Compared with idealized bubbles of the same dimensions and constant buoyancy (not shown), the tartare responses are weaker by a small fraction but otherwise exhibit similar profiles. This is consistent with the nonlocal dynamics being robust to small-scale variations and depending primarily on large-scale integral measures for the features of interest. The fine structures within the buoyant region give rise to localized intense accelerations. The effects of this on the horizontal average in Figs. 4b,d, may be seen in variations among instances of the tartare. Below the buoyant region, however, the nonlocal effects create relatively smooth structure even for individual instances. Furthermore,

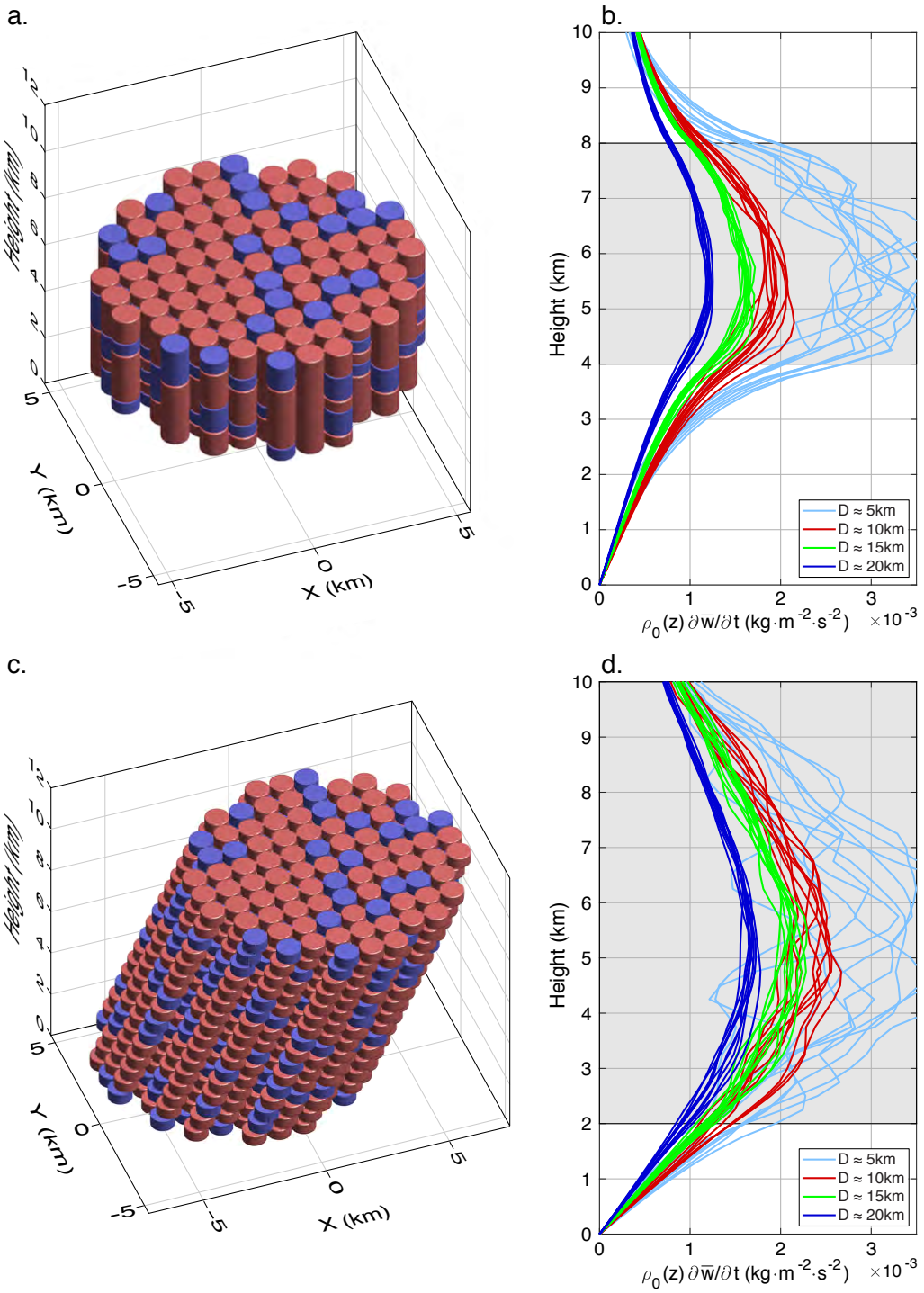

Figure 4. (a) A realization of a net-positive buoyancy tartare—an aggregate of stochastically-generated smaller positive (red) and negative (blue) buoyancy elements—of horizontal diameter $D \approx 10$ km and vertical extent $4 \leq z \leq 8$ km. Buoyancy value within individual element is approximately constant, and of equal strength for warm and cold elements. The ratio of numbers of warm to cold elements is set to 7:3. A ∼12 km region of a 64-km domain is shown. (b) Theoretical response of convective mass flux to an ensemble of 10 tartare realizations as in (a), for varying D. The average buoyancy over each tartare is rescaled to +0.01 m/s^2. Each curve represents the mean profile within the tartare diameter. (c) As in (a), with vertical extent $2 \leq z \leq 10$ km and tilt $\approx 27°$ ($\Delta z/\Delta x \equiv 2$). (d) As in (b), but for vertically tilted tartares as in (c). See *section S3* for numerical details.

this horizontal-average mass flux is equivalent to the horizontal convergence of air entering the feature, bringing in unmodified air from the far field and thus tending to dominate the effect of the environment on the feature.

5 Discussion

Aspects of nonhydrostatic nonlocal solutions have been studied in recent years with different focuses. For instance, the rate of entrainment of individual updrafts as a function of updraft size has been examined for dry plumes (Lecoanet & Jeevanjee, 2019). Relationships of entrainment and plume scale have been incorporated into recent convective parameterizations for preliminary testing (Peters et al., 2021). Such approaches are similar to modifying the idealized monochromatic response as in Fig. 3 as building blocks for constraining mass flux profiles. Although results here are aimed at explaining a feature of observations, they have implications for such parameterization efforts. In particular, they underline that the leading-order flow response to a buoyant region of a finite size includes contributions from a range of wavelengths. This is key to the robustness of nonlocal dynamics at the larger scales involved in convection—those less amenable to treatment by moment closures or traditional turbulent assumptions—especially when one has in mind the formulation for organized ensembles of smaller structures (Moncrieff et al., 2017). Superparameterizations include representations of all these effects by partially resolving them with CRMs embedded into GCM grid-boxes (Chern et al., 2016; Jansson et al., 2019; Jones et al., 2019). The nonlocal effects whose importance is emphasized here are thus likely captured, even if small-scale turbulence is not resolved—but superparameterization remains computationally expensive. Approaches such as Morrison (2017) and Lecoanet and Jeevanjee (2019) may be promising if generalized to include the nonlocal effects underlined here both vertically and horizontally. Overall, leveraging anelastic solutions such as those here can help move parameterizations away from the idealization of entrainment as determined purely locally by a single parameter.

In light of these results, what can be considered universal regarding the convective mass flux profile? Not so much a specific profile shape, but the inherent vertically and horizontally nonlocal effects tending to yield a deep contribution to the mass flux. The nonlocal dynamics is effective at integrating over heterogeneous buoyancy (as in the tartare solutions), and can generate deep inflow robustly under a wide range of conditions. Variations in the distribution of buoyancy can create departures from this. In particular, a layer of negative buoyancy can yield reductions in the vertical increase of mass flux, or even a low-level layer of negative vertical velocity at small scales. Yet because the nonlocal dynamics operates persistently, deep-inflow profiles tend to appear in averages of mass flux over many convective instances.

The observationally motivated hypothesis that there is a common explanation for the deep inflow into heavily precipitating unorganized convection and mesoscale-organized convection indeed has a simple explanation: the nonlocal dynamics entailing interaction between the buoyant layer and the surface. The robustness of this effect, especially at scales relevant for both large cumulonimbus and MCSs, supports the potential for parameterizing aspects of these systems. Although it implies the need to include nonlocal, anelastic dynamics in convective parameterizations, the overall effect is to simplify key aspects of the interaction with the thermodynamic environment for large convective entities.

Appendix A Convective precipitation feature scales and MCS identification

For convective precipitation features, we use the TRMM 2A25 data (TRMM, 2011) for the period of June 2002 through May 2014 that include PR retrievals of surface rain rate ($rain$) and type ($rainType$) at 5 km $\times$ 5 km resolution covering 40°S-40°N. The

values of *rainType* consist of three numerical digits, and here we consider 2X0 (X = 0, 2, 3, 4) convective. Note that these are different from shallow-convective and have $rain \geq$ 0.11 mm/h—the minimum detectable by the PR. For each 2A25 file (i.e., one orbit) we identify all contiguous areas and/or along-track chords consisting of convective raining pixels for the two measures of convective feature size. We further associate each area/chord with MCS or non-MCS depending on whether the feature overlaps with an MCS identified following Mohr and Zipser (1996) for simple criteria not directly dependent on precipitation: With the 10.8 μm brightness temperature (TB_{11}) from the Merged IR product (Janowiak et al., 2017), for each IR snapshot, we identify MCS as an area with $TB_{11} <$ 250 K of at least 2,000 km^2 and an enclosed minimum $<$ 225 K.

Acknowledgments

This work was supported by National Science Foundation grant AGS-1936810 and National Oceanic and Atmospheric Administration grant NA21OAR4310354. We thank J. Meyerson for graphical assistance.

Data availability statement

The TRMM 2A25 (TRMM, 2011) and Merged IR products (Janowiak et al., 2017) are maintained and provided by NASA's GES DISC publicly accessible via `https://disc.gsfc.nasa.gov/`.

References

Ahmed, F., & Neelin, J. D. (2018). Reverse engineering the tropical precipitation-buoyancy relationship. *Journal of the Atmospheric Sciences*, *75*, 1587–1608. Retrieved from `http://journals.ametsoc.org/doi/10.1175/JAS-D-17-0333.1` doi: 10.1175/JAS-D-17-0333.1

Arakawa, A., & Schubert, W. H. (1974). Interaction of a cumulus cloud ensemble with the large-scale environment, Part I. *Journal of Atmospheric Sciences*, *31*(3), 674–701.

Bretherton, C. S., Henn, B., Kwa, A., Brenowitz, N. D., Watt-Meyer, O., McGibbon, J., ... Harris, L. (2021). Correcting coarse-grid weather and climate models by machine learning from global storm-resolving simulations. *Preprint on https://www.essoar.org/*.

Bryan, G. H., & Fritsch, J. M. (2002). A benchmark simulation for moist nonhydrostatic numerical models. *Monthly Weather Review*, *130*(12), 2917–2928.

Burleyson, C. D., Feng, Z., Hagos, S. M., Fast, J., Machado, L. A., & Martin, S. T. (2016). Spatial variability of the background diurnal cycle of deep convection around the GoAmazon2014/5 field campaign sites. *Journal of Applied Meteorology and Climatology*, *55*(7), 1579–1598.

Chern, J.-D., Tao, W.-K., Lang, S. E., Matsui, T., Li, J.-L., Mohr, K. I., ... Peters-Lidard, C. D. (2016). Performance of the Goddard multiscale modeling framework with Goddard ice microphysical schemes. *Journal of Advances in Modeling Earth Systems*, *8*(1), 66–95.

Cotton, W. R., Bryan, G. H., & Van den Heever, S. C. (2010). *Storm and cloud dynamics*. Academic press.

Del Genio, A. D., & Wu, J. (2010). The role of entrainment in the diurnal cycle of continental convection. *Journal of Climate*, *23*(10), 2722–2738.

de Rooy, W. C., & Siebesma, A. P. (2010). Analytical expressions for entrainment and detrainment in cumulus convection. *Quart. J. R. Meteorol. Soc.*, *136*, 1216-1227. doi: 10.1002/qj.640

Ferrier, B. S., & Houze, R. A. (1989). One-dimensional time-dependent modeling of GATE cumulonimbus convection. *J. Atmos. Sci.*, *46*, 330–352.

Holloway, C. E., & Neelin, J. D. (2007). The convective cold top and quasi equilibrium. *Journal of the atmospheric sciences*, *64*(5), 1467–1487.

Houghton, H. G., & Cramer, H. E. (1951). A theory of entrainment in convective currents. *Journal of Atmospheric Sciences*, *8*(2), 95–102.

Houze, R. A. (1993). *Cloud Dynamics*. Academic Press.

Janowiak, J., Joyce, B., & Xie, P. (2017). *NCEP/CPC L3 Half Hourly 4km Global (60S - 60N) Merged IR V1.* Edited by Andrey Savtchenko, Greenbelt, MD, Goddard Earth Sciences Data and Information Services Center. (Accessed 7-Jan-2020) doi: 10.5067/P4HZB9N27EKU

Jansson, F., van den Oord, G., Pelupessy, I., Grönqvist, J. H., Siebesma, A. P., & Crommelin, D. (2019). Regional superparameterization in a global circulation model using large eddy simulations. *Journal of Advances in Modeling Earth Systems*, *11*(9), 2958–2979.

Jeevanjee, N. (2017). Vertical velocity in the gray zone. *Journal of Advances in Modeling Earth Systems*, *9*(6), 2304–2316.

Jeevanjee, N., & Romps, D. M. (2016). Effective buoyancy at the surface and aloft. *Quarterly Journal of the Royal Meteorological Society*, *142*(695), 811–820.

Jones, T. R., Randall, D. A., & Branson, M. D. (2019). Multiple-instance superparameterization: 1. Concept, and predictability of precipitation. *Journal of Advances in Modeling Earth Systems*, *11*(11), 3497–3520.

Jung, J.-H., & Arakawa, A. (2008). A three-dimensional anelastic model based on the vorticity equation. *Monthly weather review*, *136*(1), 276–294.

Khairoutdinov, M. F., & Randall, D. A. (2003). Cloud resolving modeling of the arm summer 1997 IOP: Model formulation, results, uncertainties, and sensitivities. *Journal of Atmospheric Sciences*, *60*(4), 607–625.

Kuang, Z., & Bretherton, C. S. (2006). A mass-flux scheme view of a high-resolution simulation of a transition from shallow to deep cumulus convection. *J. Atmos. Sci.*, *63*, 1895–1909.

Kuo, Y.-H., Neelin, J. D., Booth, J. F., Chen, C.-C., Chen, W.-T., Gettelman, A., ... Zhao, M. (2020). Convective transition statistics over tropical oceans for climate model diagnostics: GCM evaluation. *J. Atmos. Sci.*, *77*, 379-403. doi: 10.1175/JAS-D-19-0132.1

Lecoanet, D., & Jeevanjee, N. (2019). Entrainment in resolved, dry thermals. *Journal of the Atmospheric Sciences*, *76*(12), 3785–3801.

LeMone, M. A., & Zipser, E. J. (1980). Cumulonimbus vertical velocity events in GATE. Part I: Diameter, intensity and mass flux. *Journal of Atmospheric Sciences*, *37*(11), 2444–2457.

Leung, L. R., Boos, W. R., Catto, J. L., DeMott, C., Martin, G. M., Neelin, J. D., ... others (2022). Exploratory precipitation metrics: spatiotemporal characteristics, process-oriented, and phenomena-based. *Journal of Climate*, 1–55.

Li, Y., Zipser, E. J., Krueger, S. K., & Zulauf, M. A. (2008). Cloud-resolving modeling of deep convection during KWAJEX. Part I: Comparison to TRMM satellite and ground-based radar observations. *Monthly weather review*, *136*(7), 2699–2712.

Lucas, C., Zipser, E. J., & Lemone, M. A. (1994). Vertical velocity in oceanic convection off tropical Australia. *Journal of Atmospheric sciences*, *51*(21), 3183–3193.

Markowski, P., & Richardson, Y. (2011). *Mesoscale meteorology in midlatitudes* (Vol. 2). John Wiley & Sons.

Marsham, J. H., Trier, S. B., Weckwerth, T. M., & Wilson, J. W. (2011). Observations of elevated convection initiation leading to a surface-based squall line during 13 June IHOP_2002. *Monthly Weather Review*, *139*(1), 247–271.

Masunaga, H., & Luo, Z. J. (2016). Convective and large-scale mass flux profiles over tropical oceans determined from synergistic analysis of a suite of satellite observations. *Journal of Geophysical Research: Atmospheres*, *121*(13),

7958–7974.

Mohr, K. I., & Zipser, E. J. (1996). Mesoscale convective systems defined by their 85-GHz ice scattering signature: Size and intensity comparison over tropical oceans and continents. *Mon. Wea. Rev.*, *124*, 2417-2437.

Moncrieff, M. W. (1992). Organized convective systems: Archetypal dynamical models, mass and momentum flux theory, and parametrization. *Quarterly Journal of the Royal Meteorological Society*, *118*(507), 819–850.

Moncrieff, M. W., Liu, C., & Bogenschutz, P. (2017). Simulation, modeling, and dynamically based parameterization of organized tropical convection for global climate models. *Journal of the Atmospheric Sciences*, *74*(5), 1363–1380.

Moncrieff, M. W., Waliser, D. E., Miller, M. J., Shapiro, M. A., Asrar, G. R., & Caughey, J. (2012). Multiscale convective organization and the yotc virtual global field campaign. *Bulletin of the American Meteorological Society*, *93*(8), 1171–1187.

Morrison, H. (2016). Impacts of updraft size and dimensionality on the perturbation pressure and vertical velocity in cumulus convection. Part II: Comparison of theoretical and numerical solutions and fully dynamical simulations. *Journal of the Atmospheric Sciences*, *73*(4), 1455–1480.

Morrison, H. (2017). An analytic description of the structure and evolution of growing deep cumulus updrafts. *Journal of the Atmospheric Sciences*, *74*(3), 809–834.

Nesbitt, S., Cifelli, W. R., & Rutledge, S. A. (2006). Storm morphology and rainfall characteristics of TRMM precipitation features. *Mon. Wea. Rev.*, *134*, 2702–2721.

Ogura, Y., & Phillips, N. A. (1962). Scale analysis of deep and shallow convection in the atmosphere. *J. atmos. Sci*, *19*(2), 173–179.

Peters, J., Morrison, H., Zhang, G., & Powell, S. (2021). Improving the physical basis for updraft dynamics in deep convection parameterizations. *Journal of Advances in Modeling Earth Systems*, *13*(2), e2020MS002282.

Plant, R. (2010). A review of the theoretical basis for bulk mass flux convective parameterization. *Atmospheric Chemistry and Physics*, *10*(8), 3529–3544.

Randall, D., Khairoutdinov, M., Arakawa, A., & Grabowski, W. (2003). Breaking the cloud parameterization deadlock. *Bulletin of the American Meteorological Society*, *84*(11), 1547–1564.

Robe, F. R., & Emanuel, K. A. (1996). Moist convective scaling: Some inferences from three-dimensional cloud ensemble simulations. *J. Atmos. Sci.*, *53*, 3265–3275.

Romps, D. M. (2010). A direct measure of entrainment. *Journal of the Atmospheric Sciences*, *67*(6), 1908–1927.

Savazzi, A. C., Jakob, C., & Siebesma, A. P. (2021). Convective mass-flux from long term radar reflectivities over Darwin, Australia. *Journal of Geophysical Research: Atmospheres*, e2021JD034910.

Schiro, K. A., Ahmed, F., Giangrande, S. E., & Neelin, J. D. (2018). GoAmazon2014/5 campaign points to deep-inflow approach to deep convection across scales. *Proceedings of the National Academy of Sciences*, *115*(18), 4577–4582.

Sherwood, S. C., Bony, S., & Dufresne, J.-L. (2014). Spread in model climate sensitivity traced to atmospheric convective mixing. *Nature*, *505*(7481), 37.

Siebesma, A. P., Bretherton, C. S., Brown, A., Chlond, A., Cuxart, J., Duynkerke, P. G., ... others (2003). A large eddy simulation intercomparison study of shallow cumulus convection. *Journal of the Atmospheric Sciences*, *60*(10), 1201–1219.

Siebesma, A. P., Soares, P. M. M., & Teixeira, J. (2007). A combined eddy diffusivity mass flux approach for the convective boundary layer. *J. Atmos. Sci.*, *64*, 1230–1248.

Trapp, R. J. (2013). *Mesoscale-convective processes in the atmosphere.* Cambridge University Press.

TRMM. (2011). *TRMM Precipitation Radar rainfall rate and profile L2 1.5 hours V7.* Goddard Earth Sciences Data and Information Services Center. (Accessed 19-Aug-2016) doi: https://disc.gsfc.nasa.gov/datacollection/TRMM_2A25_7.html

Wing, A. A., Stauffer, C. L., Becker, T., Reed, K. A., Ahn, M.-S., Arnold, N. P., ... others (2020). Clouds and convective self-aggregation in a multimodel ensemble of radiative-convective equilibrium simulations. *Journal of advances in modeling earth systems*, *12*(9), e2020MS002138.

Yano, J.-I., & Moncrieff, M. W. (2016). Numerical archetypal parameterization for mesoscale convective systems. *Journal of the Atmospheric Sciences*, *73*(7), 2585–2602.

Supplementary Information for

Conditions for convective deep inflow

Yi-Hung Kuo & J. David Neelin

Yi-Hung Kuo
E-mail: yhkuo@atmos.ucla.edu

This PDF file includes:

Supporting Information Text

S1. Governing equation for response

In the main text, the nonlocal dynamics is studied via diagnosing the vertical acceleration in response to buoyancy using Eq. (1). Here we demonstrate how the equation can be derived from the vorticity and anelastic continuity equations.

Notations and constants. The 3D velocity and vorticity are denoted by $\mathbf{u} = (\mathbf{u}_h, w) = (u, v, w)$ and $\omega \equiv \nabla \times \mathbf{u} = (\xi, \eta, \zeta)$, respectively (subscript h for horizontal components). We use ρ and θ for atmospheric density and potential temperature, and subscript 0 for hydrostatic reference states that are time-invariant and horizontally homogeneous. Relevant constants for dry air used here include the gas constant $R_d = 287$ J/kg/K, specific heat at constant pressure $c_{pd} = 1,005$ J/kg/K and at constant volume $c_{vd} = 718$ J/kg/K (Houze, 1993). Also, $g = 9.81$ m/s^2.

Derivation. Following Jung and Arakawa (2008), from the definition of ω,

$$\begin{aligned} \partial_y \xi - \partial_x \eta &\equiv \nabla_h^2 w - \partial_z (\nabla_h \cdot \mathbf{u}_h) \\ &= \nabla_h^2 w + \partial_z \left[\frac{1}{\rho_0} \partial_z (\rho_0 w) \right]. \end{aligned} \tag{S1}$$

The last equality follows the anelastic continuity equation

$$\nabla_h \cdot (\rho_0 \mathbf{u}_h) + \partial_z (\rho_0 w) = 0.$$

Applying ∂_t to both sides of Eq. (S1) and substituting $\partial_t \xi$, $\partial_t \eta$ using the vorticity equation, it is straightforward to derive Eq. (1) with

$$\begin{aligned} B &\equiv g \left(\frac{\theta'}{\theta_0} + 0.61 q_v - q_c \right), \\ \mathcal{D} &\equiv -\frac{\partial}{\partial z} \nabla \cdot [\mathbf{u} \times (\omega + \mathbf{f})] + \nabla^2 (u\eta - v\xi), \end{aligned}$$

where B is the buoyancy, θ' the potential temperature deviation from θ_0, q_v and q_c the mixing ratios of water vapor and condensate, $\mathbf{f}$ the Coriolis parameter pointing along the z-direction. Note that $(u\eta - v\xi)$ is the z-component of $\mathbf{u} \times \omega$. It should also be noted that Eq. (1) is similar to the decomposition adopted by Jeevanjee and Romps (2016) in that both capture the nonlocal nature and have the identical response to buoyancy. $\mathcal{D}$ can become a significant modifier in strong flow regimes, but spatial filtering by the nonlocal solutions to Eq. (1) would in principle apply to forcing by $\mathcal{D}$ as well.

Atmospheric density. In practice, $\rho_0(z)$ is often determined by a prescribed reference potential temperature $\theta_0(z)$ assuming hydrostatic balance. For the current study, to facilitate our analytic approach, we assume

$$\rho_0(z) \equiv \frac{P_0}{R_d \Theta_0} \left(1 - \frac{z}{H} \right)^\beta,$$

with the reference pressure P_0 and potential temperature Θ_0 at $z = 0$ (values set to 1,000 hPa and 292.8 K so that $H \equiv c_{pd}\Theta_0/g \equiv 30$ km throughout this study), and $\beta = c_{vd}/R_d \approx 2.5$ for an isentropic atmosphere (i.e., $\theta_0 \equiv \Theta_0$). Note that the atmospheric stability can be adjusted by slightly varying β, which will not alter our key findings, and neither will a more general ρ_0.

S2. Analytic solutions

In section 3.2 of the main text, it was stated that the monochromatic (i.e., single horizontal wavelength) vertical structure of the response can be solved analytically for individual Fourier modes. To do so, we introduce the changes of variables

$$s \equiv 1 - \frac{z}{H}, \quad A(s) \equiv \sqrt{\rho_0}\, \widehat{a}, \tag{S2}$$

with which Eq. (2) becomes

$$A'' - \lambda(s)^2 A = -F(s). \tag{S3}$$

Here $(\cdot)'$ denotes d/ds, and

$$\begin{aligned} F(s) &\equiv \lambda_0^2 \sqrt{\rho_0} \widehat{B}, \\ \lambda(s) &\equiv \lambda_0 \left(1 + \frac{\gamma}{\lambda_0^2 s^2} \right)^{1/2}, \\ \lambda_0 &\equiv 2\pi H/L, \\ \gamma &\equiv \frac{\beta}{2} \left(\frac{\beta}{2} + 1 \right). \end{aligned}$$

A WKB approach gives approximate homogeneous solutions to Eq. (S3)

$$A^{\pm}(s) = e^{\mp\lambda(s)s}\left(\frac{\lambda(s)s-\sqrt{\gamma}}{\lambda(s)s+\sqrt{\gamma}}\right)^{\mp\sqrt{\gamma}/2}\lambda(s)^{-1/2}, \tag{S4}$$

leading to $\widehat{a}^{\pm}(z)$ in Eq. (3). When $\widehat{B}$ is slowly-varying, such that $O(F''/\lambda^2) \ll O(F)$, this condition allows an asymptotic approximation to the particular solution

$$A^{p}(s) = \frac{1}{\lambda(s)^2}\left[F(s)+\frac{F''(s)}{\lambda(s)^2}\right], \tag{S5}$$

leading to $\widehat{a}^{p}(z)$ in Eq. (4).

The monochromatic solutions in Fig. 3 are evaluated using Eqs. (S4) and (S5). The value and first derivative of the solutions are matched across the jumps of buoyancy in the vertical. This requires inverting regular yet ill-conditioned (because of the exponentials) linear systems for which symbolic computations are employed.

The monochromatic responses to a single layer of buoyancy at various height and for different horizontal wavelength L form a basis that is used for building responses to more general buoyancy configurations in Fig. 4. The solutions built this way are consistent with those obtained by numerically solving Eq. (1).

For general ρ_0, Eqs. (S2) and (S3) still apply though with different $\lambda(s)$ and approximate solutions.

S3. Numerical evaluations of responses

This section provides additional details for the computations of the solutions presented in Figs. 1b, 2 and 4 in the main text.

To construct the idealized buoyancy bubbles, we use the normal cumulative distribution function denoted by

$$\mathcal{N}(\tau,\tau_0,\sigma) \equiv \frac{1}{2}\,erfc(-\frac{\tau-\tau_0}{\sqrt{2}\sigma}).$$

In Fig. 2, the cylindrical bubbles of positive buoyancy (units: $\mathrm{m/s^2}$) are given by

$$B_{+}(r,z) \equiv 10^{-2}\times[1-\mathcal{N}(r,4,0.2)]\mathcal{N}(z,4,0.1)[1-\mathcal{N}(z,8,0.1)],$$

where $r \equiv \sqrt{x^2+y^2}$. Both r and z are in km. The bubbles have a horizontal diameter of 8 km, and extend vertically from 4 to 8 km (magenta contours). The negatively buoyant bubble (blue contour) resembling convective cold-top is given by

$$B_{-}(r,z) \equiv -6\cdot 10^{-2}\times[1-\mathcal{N}(r,4,1.2)]\mathcal{N}(z,8.2,0.1)[1-\mathcal{N}(z,8.5,0.1)].$$

The cold-top has the same diameter (but a more moderate transition) in the horizontal, a narrower vertical extent from 8.2 to 8.5 km, and a greater magnitude of buoyancy. For the two cases displayed in Fig. 2, instead of directly solving Eq. (1), we consider a domain doubly periodic in the horizontal $-16 \le x,\, y \le 16$ km, and separately solve Eq. (2) for $\widehat{a}(z;k,\ell)$ numerically with vanishing conditions at $z = 0$, 20 km for all admissible (k,ℓ), then reconstruct a via inverse Fourier transform. The horizontal and vertical grid spacings used are 125 and 6 m.

The tartares in Fig. 4 consist of raw elements having buoyancy of the form

$$b_{\pm} \equiv \pm\frac{1}{2}\,erfc\left(\frac{r-0.5}{0.02}\right)\mathcal{H}(z-z_B)\mathcal{H}(z_B+0.5-z),$$

with r, z, z_B in km, and $\mathcal{H}$ denoting the Heaviside function. When building a tartare of diameter $\approx D$, the $\pm$ signs are randomly assigned with $7:3$ probabilities. Then the integral buoyancy of each tartare is rescaled to that of $10^{-2}\times\frac{1}{2}\,erfc\left(\frac{r-D/2}{0.2}\right)\times\mathcal{H}(z-z_B)\mathcal{H}(z_T-z)$ (≈ 0.01 $\mathrm{m/s^2}$ on average within the tartare of diameter D and depth z_T-z_B). The overall responses to buoyancy tartares are computed utilizing the monochromatic basis in a 64 km $\times$ 64 km doubly-periodic horizontal domain with grid spacing 62.5 m. Using the analytic expressions for vertical structures (as described in section S2), the accuracy of solutions is not affected by vertical grid spacing. For tilted tartares, the tartare cross section for $5.5 \le z \le 6$ km is centered at $x = y = 0$. The profiles in Figs. 4b,d represent the mass flux responses averaged over $x^2+y^2 \le D/2$ for individual tartare realizations. The mean profiles averaged over an ensemble of 10 tartare realizations (as shown in Fig. 4b) for varying diameter D are summarized in Fig. 1b for the lower troposphere.

S4. Horizontal features of finite size and their Fourier spectrum

In section 4 of the main text, we noted the importance of the fact that net-positive buoyancy features of a finite horizontal size D consist of Fourier component contributions primarily from wavelength $L \gtrsim D$. Here we provide an analytic illustration of this and numerical examples for more realistic instances.

Analytic illustration. Consider an idealized feature of size D in a large 1D domain

$$B_H(x) \equiv \begin{cases} 1, & |x| \le D/2, \\ 0, & \text{elsewhere}, \end{cases}$$

and its Fourier coefficient (omitting the normalization factor that varies with domain size)

$$\widehat{B_H}(k) \equiv \int B_H(x) e^{-2\pi i k x} dx.$$

When $L \equiv 1/|k|$ is comparable to or smaller than D, the sign of the integrand changes. The positive and negative contributions to the integral tend to cancel, resulting in $\widehat{B_H}(k)$ of small magnitude. In contrast, when L exceeds D (or $2D$ to be conservative), the integrand tends to be of the same sign, leading to a substantial $\widehat{B_H}(k)$.

For this idealized case, the integral can be readily evaluated

$$\widehat{B_H}(k) = \begin{cases} \frac{D}{k\pi D} \sin(k\pi D), & k \neq 0, \\ D, & k = 0. \end{cases}$$

Normalize $\widehat{B_H}$ by its value at $k = 0$. The magnitude of $\widehat{B_H}$ is bounded by the envelope $1/|k|\pi D \equiv L/\pi D$, i.e., there are important contributions from all Fourier components of wavelength on the order of or larger than D. Assuming a single dominant wavelength at D can thus be highly misleading, especially for aspects where dynamics favors the longer wavelengths in the response.

More realistic illustration. In 2D, consider the idealized pattern

$$b_H(x, y) \equiv \frac{1}{2} erfc\left(\frac{r - 0.5}{0.02}\right),$$

where $r \equiv \sqrt{x^2 + y^2}$ (units: km). $b_H \approx 1$ for $r < 0.5$ km and vanishes elsewhere with a smooth transition over a width $\sim$0.06 km. In Fig. S1, the pattern of b_h and its Fourier coefficient

$$\widehat{b_H}(k, \ell) \equiv \iint b_H(x, y) e^{-2\pi i (kx + \ell y)} dx dy$$

are represented by gray lines. b_h has its primary Fourier contribution from $K \equiv \sqrt{k^2 + \ell^2} \lesssim 1$ (km^{-1}), or $L \equiv 1/K \gtrsim 1$ km.

Using b_h, we construct more complicated net-positive patterns as

$$B_H(x, y) \equiv \sum_{n=1}^{1{,}000} s_n m_n b_H(x - x_n, y - y_n),$$

where $s_n = \pm 1$ with 7:3 positive-to-negative ratio, m_n the magnitude uniformly distributed in $[0, 1]$, and (x_n, y_n) the center of b_h uniformly spread within a circle of diameter 10 km. Figure S1a shows one such realization, which seems plausible for convection. Its Fourier coefficient for $k \ge 0$, $\ell = 0$ is included in Fig. S1b (magenta thick) together with the results for nine more realizations. These examples demonstrate that when an ensemble of 1-km patterns form net-positive features of larger scale (here diameter 10 km), the primary Fourier contributions are from $K \lesssim 1/10$ (km^{-1}), or $L \gtrsim 10$ km.

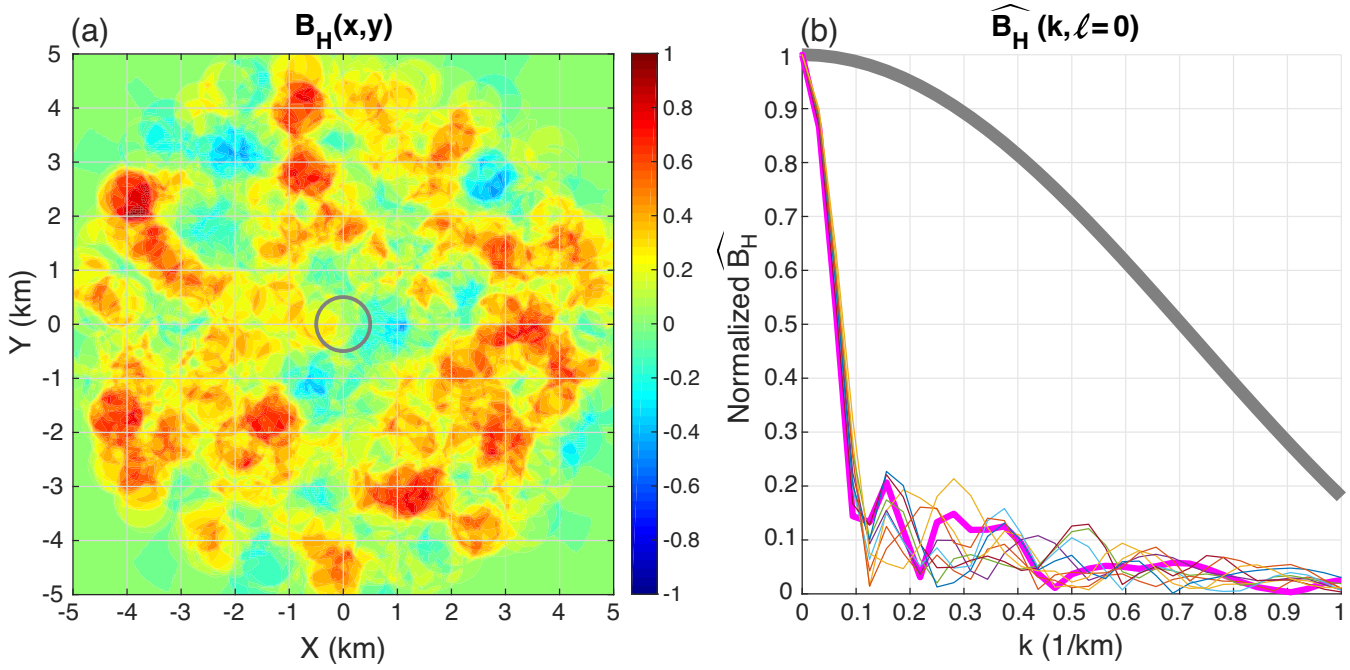

Fig. S1. (a) An idealized buoyancy pattern b_h of diameter 1 km (gray contour) and a realization of a stochastically-generated net-positive pattern of diameter $\approx$ 10 km (color shading) shown on a 10 km$\times$10 km zoom of a 32 km$\times$32 km doubly-periodic domain. The pattern is constructed using 1,000 copies of b_h, with their centers randomly spread within a circle of diameter 10 km, magnitudes uniformly distributed in $[0, 1]$, and 7:3 positive-to-negative sign ratio. (b) The Fourier coefficients of b_h (gray thick) and 10 realizations of the stochastically-generated net-positive patterns (colors) for wavenumbers $k \geq 0$, $\ell = 0$. The Fourier coefficient of the pattern in (a) is indicated by the thick magenta line. The Fourier coefficients are normalized by their values at $k = \ell = 0$.